Research Square

Preprints are preliminary reports that have not undergone peer review.
They should not be considered conclusive, used to inform clinical practice,
or referenced by the media as validated information.

Geometric control of ZnO nanorod alignment in hydrothermal synthesis without chemical modification

Sumin Kim
Daegu University
Hyun Jeong
hjeong6620@daegu.ac.kr

Daegu University

Research Article

Keywords: ZnO nanorod arrays, hydrothermal synthesis, vertical alignment, homogeneous nucleation, light extraction

Posted Date: November 13th, 2026

DOI: https://doi.org/10.21203/rs.3.rs-11528297/v1

License: This work is licensed under a Creative Commons Attribution 4.0 International License.
Read Full License

Additional Declarations: No competing interests reported.

Abstract

Vertically aligned ZnO nanorod arrays are used as antireflection and light-extraction layers on optoelectronic devices, but their alignment in hydrothermal synthesis is usually controlled through strongly coupled chemical parameters. In this study, the effect of the loading direction of the seeded substrate in the autoclave was isolated by growing upward- and downward-facing substrates side by side in a single run, so that all chemical parameters were identical. On both SiO_2/Si and GaN-based light-emitting diode (LED) substrates, the downward-facing configuration produced dense arrays of c-axis-aligned rods, 100–200 nm wide and terminated by hexagonal (0001) facets, whereas the upward-facing configuration produced randomly inclined needles a few tens of nanometers wide, accompanied by sedimented ZnO agglomerates. A Stokes-law estimate showed that particulates formed in solution settle over centimeter distances within the growth time, supporting gravitational sedimentation as the origin of this difference. On the LED substrate, the aligned array showed a resolved near-band-edge emission at 380 nm, a weaker deep-level emission, and a clearly transmitted 450 nm LED emission, which was not detected through the randomly oriented array. Its transmittance at 450 nm was 1.95 times higher, and the nearly wavelength-independent difference in extinction indicated that the gain originated mainly from reduced Mie scattering rather than from index matching. These results show that the substrate loading direction is a significant growth parameter that should be controlled and reported in the hydrothermal synthesis of ZnO nanorod arrays.

1 Introduction

Zinc oxide (ZnO) is one of the most extensively studied wide-bandgap semiconductors. Its direct bandgap of 3.37 eV and its unusually large exciton binding energy of 60 meV enable excitonic processes to occur at room temperature [1, 2]. Its transparency across the visible spectrum, as well as its chemical and thermal stability, piezoelectric response, and low toxicity, makes ZnO attractive for use in practical devices [3–6]. These properties have been exploited in ultraviolet photodetectors, light-emitting diodes, transparent conducting layers, gas sensors, and piezoelectric energy harvesters [7–9]. Among the various ZnO morphologies, vertically aligned one-dimensional nanorod arrays are of particular interest [10–12]. These arrays combine a large surface-to-volume ratio with continuous, defect-tolerant transport paths along their axes. Their effective refractive index is intermediate between those of typical device materials and that of air. Thus, a vertically aligned array placed on a light-emitting structure can simultaneously act as an antireflection layer and a light-extraction layer [13–15]. A wide range of techniques has been used to prepare ZnO nanostructures, including chemical vapor deposition, molecular beam epitaxy, sputtering, sol-gel processing, and electrodeposition. Among these methods, hydrothermal synthesis occupies a distinct position because it proceeds in an aqueous solution at temperatures typically below 150°C [16–18]. This method requires no vacuum equipment and can be scaled to large areas at a low cost. This low thermal budget is especially valuable when integrating ZnO onto completed devices, such as finished GaN-based light-emitting diodes, flexible substrates, or structures containing metal contacts, which can tolerate a 120°C aqueous process but not high-temperature vapor-phase growth. Thus, hydrothermal growth is the preferred method for adding

functional ZnO nanorod layers to existing optoelectronic devices. The primary challenge of this approach is controlling the alignment and crystalline quality of the resulting rods. Vertical alignment is influenced by the texture of the seed layer, precursor concentration, solution pH, reaction temperature and time, and choice of structure-directing additives, such as hexamethylenetetramine or polyethyleneimine [18, 19]. These variables are strongly coupled; a change in one generally requires re-optimization of the others. Modest deviations in pH or concentration can shift the product from well-aligned rods to inclined needles to disordered aggregates [20, 21]. Optimizations obtained for one substrate often do not transfer to another because nucleation density depends on the substrate itself [22, 23]. Additionally, structure-directing additives can leave residual impurities that act as recombination centers [24, 25]. This is a significant drawback when the layer is intended for optical use. A further factor is usually addressed only implicitly. In a sealed autoclave, heterogeneous nucleation on the seeded substrate and homogeneous nucleation in the bulk solution occur simultaneously, and the ZnO formed in solution can itself participate in growth at the substrate. Suspended particulates can reach the growth surface and act as randomly oriented secondary nuclei. This contribution is usually suppressed indirectly by diluting the solution, shortening the reaction time, or adding capping agents. Each of these measures alters the growth kinetics simultaneously. A purely geometric precaution has also been adopted: in several solution-growth protocols the substrate is suspended or floated face-down so that precipitates cannot fall onto it [26, 27], and longer rods have been reported on the downward-facing side of immersed substrates [28]. In these reports, however, the face-down geometry was used as a practical precaution or observed incidentally, and its effect on alignment, facet development, and optical properties has not been isolated in a comparison in which the loading direction is the only variable. What has been lacking is therefore a controlled, quantitative assessment of how much this geometric variable alone contributes to the alignment and optical quality of the array.

In this study, the effect of this geometric variable, the direction in which the seeded substrate is loaded into the reactor, was isolated and quantified. Because ZnO formed in solution is denser than the medium and settles under gravity, the orientation of the growth surface is expected to determine whether these particulates accumulate on the seed layer or are transported away from it. The novelty of this work over previous reports on hydrothermal ZnO nanorod arrays is threefold. First, the loading direction was treated as the sole experimental variable: upward- and downward-facing substrates were grown side by side in the same reactor during a single run, which excludes run-to-run variation, whereas earlier studies adopted face-down loading only as a practical precaution without isolating its effect [26, 27]. Second, the comparison was carried out on both an amorphous SiO_2/Si substrate and a device-relevant GaN-based light-emitting diode (LED) substrate. Third, the structural difference was linked quantitatively to the optical function of the array, namely the transmission of the underlying LED emission, and the underlying loss mechanism and growth mechanism were analyzed with simple physical models of light scattering and particle sedimentation.

2 Experimental Methods

2.1 Materials and substrates

Zinc acetate dihydrate ($Zn(CH_3COO)_2{\cdot}2H_2O$, M = 219.51 g mol^{-1}), high-purity ethanol, and ammonia solution were used as received without further purification. Deionized (DI) water was used throughout. Double-side-polished fused quartz slides, thermally oxidized SiO_2/Si wafers, and commercial GaN-based LED wafers with a peak emission wavelength of approximately 450 nm were used as substrates. Prior to seeding, the substrates were cleaned by sequential ultrasonication in acetone, ethanol, and DI water, and were then dried under a stream of dry air.

2.2 Hydrothermal synthesis of ZnO nanorods

The ZnO seed solution was prepared by dissolving 0.219 g of $Zn(CH_3COO)_2{\cdot}2H_2O$ in 200 mL of high-purity ethanol (0.005 M), followed by 5 min of manual shaking and 20 min of ultrasonication. The seed solution was drop-coated onto the cleaned substrate, held for 20 s, rinsed with ethanol, and dried with an air gun; this cycle was repeated five times. The seeded substrate was then baked on a hot plate at 300°C for 20 min to thermally decompose the deposited precursor into crystalline ZnO seeds. The growth solution was prepared by dissolving 2.19 g of $Zn(CH_3COO)_2{\cdot}2H_2O$ in 200 mL of DI water (0.05 M) in a beaker sealed with Parafilm and stirred at 500 rpm for 20 min. Its pH was raised to 9 by adding ammonia solution dropwise under stirring while monitoring with a pH meter. The seeded substrate was fixed on a holder and placed in a Teflon reactor, which was then completely filled with the growth solution to minimize the free volume. The reactor was sealed in a stainless-steel autoclave and held in a preheated oven at 120°C for 1 h. After the reaction, the sample was rinsed with ethanol and dried with an air gun. Two sets of samples were prepared under otherwise identical conditions and differed only in the orientation of the substrate inside the reactor: the seed layer was loaded facing upward for one and facing downward for the other. The two substrates were mounted side by side at the same height on a single Teflon holder, separated by approximately 2 cm, and were grown simultaneously in one run, so that they shared a single growth solution and a single temperature history. Mounting them at the same height ensures that any vertical gradient in supersaturation or in particulate concentration within the reactor acted equally on both, leaving the direction of the growth surface as the only difference between them, and no comparison in this work relies on reproducibility between separate runs. The experiment was repeated more than ten times under these conditions with consistent results. The same procedure was applied to both the SiO_2/Si and the GaN-based LED substrates.

2.3 Characterization

The surface morphology of the ZnO nanorods was examined by field-emission scanning electron microscopy (FE-SEM; Hitachi S-4800). Both top-view and perspective-view images were acquired at an accelerating voltage of 15 kV. Photoluminescence (PL) measurements were performed at room temperature. A continuous-wave He–Cd laser operating at 325 nm was used as the excitation source and was focused onto the sample surface with an excitation power of 5 mW. The emitted light was collected in a backscattering configuration, dispersed by a monochromator with a focal length of 30 cm,

and detected with a Si charge-coupled device (CCD) detector (PIXIS 100, Teledyne Princeton Instruments). A long-pass filter was placed in front of the entrance slit to reject the scattered laser line. The reference spectrum of the bare GaN-based LED structure was recorded under identical excitation and collection conditions, and all spectra are presented in arbitrary units without normalization. Raman scattering measurements were carried out at room temperature using a confocal Raman spectrometer (NTEGRA Spectra, NT-MDT) with a 532 nm laser as the excitation source in a backscattering geometry. The laser was focused onto the sample surface through a ×20 objective lens, and the excitation power was kept below 0.1 mW to avoid laser-induced heating. The spectral resolution was better than 0.1 cm − 1, and the spectrometer was calibrated using the first-order Raman peak of a Si reference at 520.5 cm^{-1}. The two samples were measured under identical conditions so that their spectra could be compared directly. Optical absorption spectra were recorded at room temperature over the 200–800 nm range using a UV–visible/NIR spectrophotometer (JASCO) in a straight-through transmission geometry, without an integrating sphere. These measurements were performed on companion nanorod arrays grown on double-side-polished fused quartz, since neither the SiO2/Si nor the GaN-based LED substrate transmits over this range, and a bare quartz slide was used as the reference. Because no integrating sphere was used, light scattered out of the collection direction is recorded together with true absorption. The reported absorbance is therefore an extinction that includes scattering losses rather than a pure absorption coefficient. This is the quantity of interest here, since the array is intended to transmit light emitted from an underlying device into a defined collection direction.

3 Results and Discussion

3.1 Effect of the seed-layer loading direction on ZnO nanorod growth

Figure 1 compares ZnO nanorods that were hydrothermally grown on SiO_2/Si substrates using two different loading geometries of the seed-layer substrate inside the autoclave. Figures 1(a) and 1(d) show schematic cross-sections of the reaction vessel consisting of a stainless-steel autoclave and a Teflon reactor liner. In these figures, the seed layer is oriented facing upward and downward, respectively. The two substrates were mounted in the same reactor and grown in a single run, so that the composition and concentration of the precursor, the solution pH, and the temperature and time histories were necessarily identical rather than merely nominally matched; the loading direction was the only variable. When the seed layer faced upward, the resulting nanorods showed no preferential orientation with respect to the normal of the substrate, as illustrated schematically in Fig. 1(b). The corresponding perspective-view field emission scanning electron microscopy (FE-SEM) image (Fig. 1(c)) reveals needle-like rods with tapered tips, lateral dimensions of a few tens of nanometers, and a broad distribution of inclination angles. The areal density of rods emerging from the surface is comparatively low, and sedimented agglomerates of solution-grown ZnO are present between them. This morphology is representative of the entire substrate, as shown by the lower-magnification images in Figs. S1(a) and S1(b) of Online Resource 1 and by the additional high-magnification images in Figs. S1(c) and S1(d). In contrast, the

sample with the seed layer facing downward (Fig. 1(e)) consists of a dense array of rods aligned close to the substrate normal. The corresponding top-view FE-SEM image (Fig. 1(f)) shows uniform, well-defined, hexagonal top facets with lateral dimensions of approximately 100–200 nm. This indicates that the rods are terminated by (0001) planes and that the c-axis lies close to the substrate normal (Figs. S2(a) and S2(c)). The degree of out-of-plane alignment was assessed from the FE-SEM images, that is, from the development of hexagonal (0001) top facets and from the spread of rod inclinations visible in the perspective views. These images probe the emergent rods directly. Conventional θ–2θ X-ray diffraction was not used for this purpose, because the ZnO (002) reflection (2θ ≈ 34.4°) coincides with the GaN (0002) reflection (2θ ≈ 34.6°) of the LED wafer, so that on the device-relevant substrate the texture of the array cannot be separated from that of the substrate, and because a θ–2θ scan of the upward-grown sample would average over the aligned seed-layer rods and the sedimented agglomerates alike. The wurtzite phase of both arrays was instead confirmed by Raman spectroscopy (Section 3.3). These morphological differences can be explained by the relative contributions of heterogeneous nucleation on the seed layer and homogeneous nucleation in the growth solution [29, 30]. During the hydrothermal decomposition of the zinc precursor, ZnO forms on the seeded surface and as suspended particulates within the solution. Since these two configurations differ only in the orientation of the growth surface relative to gravity, the loading direction determines whether the homogeneously nucleated species can reach the growth front. In the case of upward-facing geometry, the precipitates settle onto the substrate. There, they act as randomly oriented secondary nuclei and simultaneously mask the underlying seed layer (Figs. S1(a) and S1(b)); the masking accounts for the lower areal density of rods emerging from the upward-grown surface despite the additional nucleation sites. Consequently, growth proceeds from a mixture of textured and randomly oriented nuclei, and the crystallographic registry provided by the seed layer is largely lost. In the downward-facing geometry, sedimentation transports particulates away from the growth surface. This results in growth dominated by heterogeneous nucleation on the seed layer, preserving the initial out-of-plane texture throughout the reaction. This interpretation aligns with the observation that the growth habit remains unchanged; both samples consist of wurtzite rods elongated along the c-axis. Only the degree of alignment, rod density, and facet development differ. Buoyancy-driven convection during the initial heating transient is expected to partially redistribute the suspended particulates; the description above applies to the subsequent isothermal period, which accounts for most of the reaction time.

This interpretation can be checked against the settling behavior of the particulates. For a sphere of radius r, the Stokes settling velocity is $v = 2(\rho_{ZnO} - \rho_w)gr^2/9\mu$. Taking $\rho_{ZnO} = 5.61$ g cm^{-3} and, for water at 120°C, $\rho_w \approx 0.94$ g cm^{-3} and $\mu \approx 0.23$ mPa s, a particle with r = 0.5 μm settles at about 11 μm s^{-1}, that is, about 4 cm during the 1 h growth, whereas its Brownian displacement over the same period is only about 0.2 mm. The micrometer-scale agglomerates in Fig. S1 settle more than an order of magnitude faster. Sedimentation therefore dominates the transport of all but the smallest particulates over distances comparable to the reactor dimensions: particulates formed above an upward-facing substrate are deposited on it, whereas a downward-facing growth surface is shielded from them. This picture is consistent with the practice of suspending or floating substrates face-down to keep precipitates off the

growth surface [26, 27] and with two direct observations in the present samples: sedimented agglomerates that are not crystallographically connected to the seed layer were found only on the upward-facing surfaces (Figs. S1 and S2), and the growth habit of the individual rods was unchanged between the two configurations.

3.2 ZnO nanorod growth on GaN-based LED substrates

To determine whether the same behavior occurs on a device-relevant substrate, the two loading geometries were applied to GaN-based LED wafers under identical synthesis conditions (see Figs. 2(a) and 2(d)). For the upward-facing configuration, the top-view and perspective-view FE-SEM images in Figs. 2(b) and 2(c) show randomly inclined rods with tapered tips that closely resemble the morphology obtained on SiO_2. The corresponding images in Figs. 2(e) and 2(f) show rods aligned along the substrate normal with hexagonal top facets for the downward-facing configuration. Because Figs. 2(b) and 2(e) were both recorded in top view and Figs. 2(c) and 2(f) in perspective view at the same magnification, Fig. 2 also provides a same-geometry comparison of the two configurations, complementing the overview images in Fig. 1. Another difference is observed in the downward-grown sample on GaN. Neighboring rods partially coalesce to form laterally merged domains with flat top surfaces, which are separated by residual voids (Figs. S2(b) and S2(d)), in contrast to the discrete rods obtained on SiO_2 (Figs. S2(a) and S2(c)). This is attributed to the structural similarity between the two wurtzite materials, ZnO and GaN. ZnO and GaN have the same crystal structure and in-plane lattice constants of a = 3.25 Å and a = 3.19 Å, respectively. This corresponds to a mismatch of approximately 1.8% [2, 31]. This small mismatch promotes a high density of nuclei aligned not only along the c-axis, but also azimuthally with respect to the GaN lattice [15]. This allows adjacent rods to merge laterally as they thicken without forming high-angle grain boundaries. Thus, the substrate governs the extent of lateral coalescence, while the loading direction determines whether the array is vertically aligned.

3.3 Photoluminescence and Raman characterization

The optical and vibrational properties of the ZnO nanorods grown on the GaN-based LED substrates are summarized in Fig. 3. Figure 3(a) compares the photoluminescence (PL) spectra of the two samples with the reference spectrum of the bare GaN-based LED structure. The same spectra are shown individually on a logarithmic scale in Fig. 3(b). In this geometry, the ~ 450 nm emission of the LED structure is generated beneath the nanorod layer and must propagate through it before detection. Therefore, the measured spectra contain information on both the intrinsic luminescence of the ZnO nanorods and their optical transparency at the LED emission wavelength. The upward-grown sample exhibits two broad bands centered at approximately 410 and 570 nm. The latter is more than 100 nm wide, so its center is quoted only to within about 10 nm. Meanwhile, the near-band-edge (NBE) emission of ZnO at around 380 nm remains unresolved. These broad bands are attributed to deep-level emissions associated with intrinsic point defects in ZnO, which are typically observed in hydrothermally grown materials [32, 33]. Additionally, the 450 nm band of the underlying LED structure is not discernible in this spectrum, indicating that the LED's emission is strongly attenuated within the randomly oriented nanorod

layer. The downward-grown sample shows a markedly different spectrum. A distinct NBE peak appears at approximately 380 nm, the deep-level band near 570 nm is comparatively weak, and the 450 nm band of the LED structure is clearly resolved and dominates the spectrum. The larger NBE-to-deep-level intensity ratio indicates a lower concentration of optically active defects, suggesting improved crystal quality in the downward-grown nanorods. It should be noted that the denser aligned array absorbs a larger fraction of the 325 nm excitation before it reaches the underlying LED, so the observed enhancement of the 450 nm band represents a lower bound on the improvement in extraction efficiency. Note that the spectra in Fig. 3(a) are plotted in arbitrary units without normalization so that comparisons can be made between the intensities of different spectral features rather than between the absolute intensities of different samples. Raman spectra of the same samples are compared in Fig. 3(c). The spectra are shown individually in Fig. 3(d). Both spectra exhibit the E_2^{high} mode of ZnO at approximately 438 cm^{-1}, as well as weak features near 380 and 410 cm^{-1}. These features are consistent with the A_1(TO) and E_1(TO) modes of wurtzite ZnO. This confirms the formation of the wurtzite phase in both samples [34]. The E_2^{high} and A_1(LO) modes of the GaN substrate are also observed at approximately 568 and 734 cm^{-1}, respectively. Since the intensity of the GaN-related modes is essentially identical for the two samples, these peaks serve as an internal reference for the excitation and collection conditions [35]. The ZnO signal can therefore be normalized to this reference as

$$\rho = \frac{I_{E_2}^{high}(ZnO)}{I_{E_2}^{high}(GaN)}$$

1

so that ρ isolates the response of the nanorod layer from variations in excitation and collection efficiency. Based on this, the higher E_2^{high} (ZnO) intensity measured for the downward-grown sample is attributable to the nanorod layer itself. The E_2^{high} mode is a non-polar phonon mode, and its intensity and linewidth are sensitive to crystalline order [36]. In backscattering geometry, its intensity additionally depends on the orientation of the c-axis relative to the incident polarization, although this dependence is strongly diluted in a rod array because scattering from the rod sidewalls contributes to the collected signal in either configuration [37]. The enhanced E_2^{high} signal is consistent with a higher density of c-axis-aligned ZnO probed in this geometry, which is in agreement with the FE-SEM results. Because the aligned array also contains more ZnO within the probe volume, the integrated intensity alone does not distinguish crystalline quality from the amount of probed material. The linewidth of this mode, which is insensitive to the probed volume, provides an independent measure: full widths at half maximum of 8.12 and 8.40 cm^{-1} were obtained for the upward- and downward-grown samples, respectively. The two values are closely similar, differing by 3.4%, and the peak positions coincide. Within the sensitivity of this measurement the short-range crystalline order and the residual strain state of the two arrays are therefore comparable. The enhanced E_2^{high} intensity of the downward-grown sample is therefore attributed to the larger amount of c-axis-aligned ZnO probed in the backscattering geometry rather than

to a difference in lattice quality. Consistent with this, the weak A_1(TO) and E_1(TO) features near 380 and 410 cm^{-1}, which are formally forbidden in backscattering from a c-plane surface, appear with comparable relative intensity in the two samples: after baseline subtraction their combined intensity amounts to 0.26 and 0.29 of the E_2^{high} intensity for the downward- and upward-grown arrays, respectively. The slightly lower value for the aligned array is in the expected direction but is not significant. The Raman response of these arrays therefore reports on the local crystal structure rather than on the out-of-plane texture, and the assessment of alignment rests on the electron microscopy data. No measurable shift in the position of the E_2^{high} peak was observed between the two samples, indicating that their residual strain states are also comparable. Taken together, the identical linewidths and peak positions show that the short-range crystalline order of the two arrays is equivalent. This is not in conflict with the photoluminescence data in Fig. 3(a): the phonon linewidth probes lattice order and phonon lifetime, whereas the deep-level emission probes the concentration of optically active point defects, and the two need not correlate.

3.4 Optical extinction and light propagation through the nanorod array

The optical response of the two nanorod arrays was examined further by measuring their absorbance over the 200–800 nm range on companion samples grown on fused quartz (Fig. 4). The measurement was made in a straight-through transmission geometry, so that light scattered out of the collection direction contributes to the measured absorbance together with true absorption. Figure 4(a) shows that the upward-grown sample has an absorbance that decreases monotonically from about 1.17 at 200 nm to about 1.11 at 800 nm. In contrast, the downward-grown sample has the same overall spectral shape, but the values are lower, ranging from about 0.87 to about 0.83. Thus, the two spectra are nearly parallel and differ by an offset of about 0.29, which is almost wavelength-independent. Neither spectrum displays a pronounced absorption edge near the ZnO band gap (3.37 eV, corresponding to 368 nm) [2]. This indicates that the measured extinction is dominated by scattering and reflection losses within the nanorod array rather than by interband absorption of ZnO; at the extinction levels recorded here the additional above-gap absorption of the rods produces no resolvable step on top of the scattering background. Accordingly, the difference between the two samples reflects a difference in optical scattering associated with morphology and alignment rather than a change in the intrinsic absorption of the material. For the same reason, a Tauc analysis of these straight-through spectra would not yield a meaningful optical bandgap. The bandgap is, moreover, not expected to depend on the loading direction: the near-band-edge emission of the aligned array at approximately 380 nm (3.26 eV) is typical of ZnO at room temperature [2, 32], and the identical E_2□□□□ peak positions and linewidths of the two arrays (Section 3.3) indicate the same crystal phase and strain state. Figure 4(b) shows magnified spectra in the LED emission region. The absorbance is approximately 1.14 at 450 nm for the upward-grown sample and 0.85 for the downward-grown sample. Writing the measured absorbance as $A = -\log_{10} T$, the ratio of

transmitted intensities at the LED emission wavelength follows directly from the offset between the two spectra,

$$\frac{T_{\mathrm{down}}}{T_{\mathrm{up}}} = 10^{A_{\mathrm{up}} - A_{\mathrm{down}}} = 10^{0.29} = 1.95$$

2

so that the vertically aligned array transmits almost twice the intensity of the randomly oriented one at 450 nm. This is consistent with the PL data in Fig. 3, in which the 450 nm emission of the underlying LED structure is resolved for the downward-grown sample but not for the upward-grown one. The near-parallel offset between the two spectra can also be used to identify the loss mechanism. Decomposing the extinction into absorptive and scattering contributions over an array thickness *d* [38],

$$A\left(\lambda\right) = \frac{d}{\ln 10}\left[\alpha_{\,\mathrm{abs}}\left(\lambda\right) + \alpha_{\,\mathrm{sca}}\left(\lambda\right)\right] + A_R$$

3

where A_R accounts for reflection at the array boundaries. Since neither spectrum shows a band-edge feature at 368 nm, α_{abs} is negligible below the gap, and the difference between the two samples is governed by $\Delta\alpha_{sca}$. For scatterers much smaller than the wavelength, the Rayleigh limit gives $\alpha_{sca} \propto Na^6\lambda^{-4}$, which would make ΔA vary by a factor of $(800/200)^4 = 256$ across the measured range. The observed values, $\Delta A = 0.30$ at 200 nm and 0.28 at 800 nm, differ by less than 10%. The excess extinction of the upward-grown sample is therefore achromatic, as expected once the size parameter [38]

$$x = \frac{2\pi\, a\, n_m}{\lambda}$$

4

approaches unity ($x \approx 1.4$ for $a = 100$ nm at $\lambda = 450$ nm, where n_m is the refractive index of the surrounding medium), placing the rods and the sedimented agglomerates in the Mie rather than the Rayleigh regime. Schematic representations of light propagation through the two arrays are shown in Figs. 4(c) and 4(d). In the randomly oriented array (Fig. 4(c)), the rods are inclined at various angles, which results in a wide range of scattering cross-sections and interfaces with the light emitted from the underlying LED. Consequently, a significant portion of the emission is scattered laterally or redirected back toward the substrate, where it can be reabsorbed. In contrast, the vertically aligned array (Fig. 4(d)) forms a quasi-continuous, periodic-in-height medium whose refractive index gradually varies between that of GaN and air. The axes of this medium are parallel to the direction of light extraction. This configuration reduces reflection at the interface and lateral scattering. Consequently, a larger fraction of the emitted light propagates through the array. This graded-index behavior can be quantified. For light

propagating along the rod axis through a subwavelength array of fill factor f_V, the zeroth-order effective index is [39, 40]

$$n_{\mathrm{eff}} = \sqrt{f_V n_{\mathrm{ZnO}}^2 + (1 - f_V)\, n_{\mathrm{air}}^2}$$

5

Reflection at the GaN/air interface is minimized when $n_{\mathrm{eff}} = (n_{\mathrm{GaN}} \cdot n_{\mathrm{air}})^{1/2}$. Taking $n_{\mathrm{GaN}} = 2.45$ [41] and $n_{\mathrm{ZnO}} = 2.03$ [42] at 450 nm gives an optimum effective index of 1.57 and a corresponding fill factor of $f_V \approx 0.46$. Evaluating the Fresnel reflectance $R = [(n_1 - n_2)/(n_1 + n_2)]^2$ at the two interfaces, the direct GaN/air reflectance of 17.7% is reduced to 9.3%, corresponding to a transmission gain of only about 1.10. The rod pitch, estimated from the FE-SEM images to be 200–300 nm, is comparable to $\lambda/n_{\mathrm{GaN}} \approx 184$ nm, so that Eq. (5) is an approximation at the boundary of the subwavelength regime [43]. It also assumes an idealized array of uniform, discrete rods; the partial lateral coalescence observed on GaN (Fig. 2(e)) makes f_V an effective rather than a geometrically exact quantity. In addition, the rod length exceeds the wavelength, so the array acts as an incoherent graded medium rather than a quarter-wave coating. Within these limits, index matching accounts for only a small part of the factor of 1.95 obtained in Eq. (2), and the remainder must originate from the suppression of lateral scattering and back-redirection described above. The correspondence between the reduced extinction in Figs. 4(a) and 4(b), the clear transmission of the LED band in Fig. 3, and the structural differences observed in Figs. 1 and 2 indicates that the alignment of the nanorods rather than a change in the composition or phase of the material governs the optical behavior of these structures. Taken together, these results show that the orientation of the seed-layer substrate during hydrothermal synthesis is sufficient to control the vertical alignment, facet development, optically active defect density, and optical transmission of ZnO nanorod arrays without altering any chemical growth parameters. This behavior was reproduced on both amorphous SiO_2/Si and single-crystalline GaN-based LED substrates, indicating that the effect originates from the growth configuration rather than the substrate type.

3.5 Implications for device applications

The two morphologies obtained here are suited to different applications. The vertically aligned, faceted array formed on the downward-facing substrate transmitted nearly twice as much of the 450 nm LED emission and showed a weaker deep-level emission. It is therefore the appropriate choice for antireflection and light-extraction layers on LEDs [15] and for devices that rely on carrier transport or light guiding along the rod axis, such as vertically integrated ultraviolet photodetectors [11]. The randomly inclined, needle-like array formed on the upward-facing substrate scatters light strongly and almost independently of wavelength over the 200–800 nm range (Fig. 4(a)) and has an open, disordered structure with tapered tips. These properties are disadvantageous for light extraction but can be useful where diffuse scattering or an exposed surface is required, for example in light-trapping layers, gas

sensors, and photocatalytic surfaces [1, 9]. The loading direction therefore provides a simple means of selecting between the two morphologies from the same growth solution.

4 Conclusion

The loading direction of the seeded substrate in the autoclave was identified as a decisive parameter in the hydrothermal growth of ZnO nanorod arrays. Under identical chemical conditions in a single run, downward-facing loading produced c-axis-aligned arrays terminated by (0001) facets on both SiO_2/Si and GaN-based LED substrates, whereas upward-facing loading produced randomly inclined needles accompanied by sedimented ZnO agglomerates, in line with the gravitational settling of particulates formed in solution. On the LED substrate, the aligned array exhibited a weaker deep-level emission and a 1.95-fold higher transmittance at the 450 nm emission wavelength, which was attributed mainly to reduced Mie scattering. The orientation of the growth surface relative to gravity should therefore be controlled and reported in hydrothermal syntheses of ZnO nanorod arrays.

Declarations

Competing interests

The authors declare no competing interests.

Author Contribution

Hyun Jeong conceived and designed the study, developing the growth methodology. Sumin Kim carried out the measurements, data analysis, and prepared the figures. Hyun Jeong contributed to the synthesis, measurements and to the interpretation of the data, provided resources and funding, and supervised and administered the project. Sumin Kim wrote the first draft of the manuscript, which was then reviewed and revised by Hyun Jeong. All authors read and approved the final manuscript, and all agree to be accountable for all aspects of the work.

Data availability

The data that support the findings of this study are available from the corresponding author upon reasonable request.

References

1. M.R. Ahmad, A.A. Ansari, M. Dhayal, R. Lv, Renew. Sustain. Energy Rev. 219, 115767 (2025). https://doi.org/10.1016/j.rser.2025.115767

2. Ü. Özgür, Ya.I. Alivov, C. Liu, A. Teke, M.A. Reshchikov, S. Doğan, V. Avrutin, S.-J. Cho, H. Morkoç, J. Appl. Phys. 98, 041301 (2005). https://doi.org/10.1063/1.1992666
3. M.A. Signore, S.K. Padmanabhan, L. Velardi, A. Serra, M. Stoppa, L. Francioso, A. Licciulli, Appl. Surf. Sci. 692, 162734 (2025). https://doi.org/10.1016/j.apsusc.2025.162734
4. J. Wang, S. Liu, X. Zhang, Y. Hou, Y. Liu, X. Li, H. Wang, Chem. Eng. J. 510, 161818 (2025). https://doi.org/10.1016/j.cej.2025.161818
5. Z. Cai, J. Hou, J.-H. Kim, G. Li, C.H. Lee, H. Kim, M. Hilal, Ceram. Int. 51, 40637 (2025). https://doi.org/10.1016/j.ceramint.2025.06.302
6. Z. Li, J. Li, M. Xiong, J. Lei, Y. Chen, S. Zhang, Appl. Surf. Sci. 584, 152588 (2022). https://doi.org/10.1016/j.apsusc.2022.152588
7. N.P. Klochko, K.S. Klepikova, I.V. Khrypunova, V.R. Kopach, I.I. Tyukhov, S.I. Petrushenko, S.V. Dukarov, V.M. Sukhov, M.V. Kirichenko, A.L. Khrypunova, Sol. Energy 232, 1 (2022). https://doi.org/10.1016/j.solener.2021.12.051
8. S. Wang, S. Liu, T. Wang, J. Bai, J. Peng, H. Zhang, W. Xie, W. Ji, Light Sci. Appl. 14, 196 (2025). https://doi.org/10.1038/s41377-025-01867-1
9. M.A. Franco, P.P. Conti, R.S. Andre, D.S. Correa, Sens. Actuators Rep. 4, 100100 (2022). https://doi.org/10.1016/j.snr.2022.100100
10. A.A.M. Raub, R. Bahru, S.N.A.M. Nashruddin, J. Yunas, J. Nanopart. Res. 26, 186 (2024). https://doi.org/10.1007/s11051-024-06098-w
11. M.R. Maurya, V. Toutam, Nanotechnology 30, 085704 (2019). https://doi.org/10.1088/1361-6528/aaf545
12. X. Huang, H. Zhang, M. Liu, Y. Miao, Z. Yu, Q. Wu, L. Pan, Acta Phys.-Chim. Sin. 42, 100293 (2026). https://doi.org/10.1016/j.actphy.2026.100293
13. Y.J. Kim, Y. Lee, D. Kim, ACS Appl. Eng. Mater. 3, 3690 (2025). https://doi.org/10.1021/acsaenm.5c00702
14. K. An, C. Kim, S. Kim, T. Lee, D. Shin, J. Lim, D. Hahm, W.K. Bae, J.Y. Kim, J. Kwak, J. Kim, K. Kang, Small 19, 2206133 (2023). https://doi.org/10.1002/smll.202206133
15. H. Jeong, D.J. Park, H.S. Lee, Y.H. Ko, J.S. Yu, S.-B. Choi, D.-S. Lee, E.-K. Suh, M.S. Jeong, Nanoscale 6, 4371 (2014). https://doi.org/10.1039/C3NR06584G
16. M. Anujency, M. Mohamed Ibrahim, S. Vinoth, V. Ganesh, R. Ade, J. Photochem. Photobiol. A 449, 115379 (2024). https://doi.org/10.1016/j.jphotochem.2023.115379
17. L. Zhu, Y. Xiang, Y. Liu, K. Geng, R. Yao, B. Li, Sens. Actuators A 341, 113552 (2022). https://doi.org/10.1016/j.sna.2022.113552
18. D. Kuang, Y. Li, Y. Gao, J. Guo, X. Li, S. Xu, B. Liu, X. Liu, Y. Zhang, Z. Yu, J. Alloys Compd. 899, 163185 (2022). https://doi.org/10.1016/j.jallcom.2021.163185
19. R. Torkamani, B. Aslibeiki, H. Naghshara, M. Darbandi, Opt. Mater. 127, 112295 (2022). https://doi.org/10.1016/j.optmat.2022.112295

20. M. Xu, Z. Yuan, B. Wang, F. Nie, J. He, X. Wang, N. Xu, J. Electron. Mater. 51, 7020 (2022). https://doi.org/10.1007/s11664-022-09931-x
21. R. Shi, P. Yang, X. Dong, Q. Ma, A. Zhang, Appl. Surf. Sci. 264, 162 (2013). https://doi.org/10.1016/j.apsusc.2012.09.164
22. J. Yang, J. Lang, C. Li, L. Yang, Q. Han, Y. Zhang, D. Wang, M. Gao, X. Liu, Appl. Surf. Sci. 255, 2500 (2008). https://doi.org/10.1016/j.apsusc.2008.07.124
23. N.S. Ridhuan, K. Abdul Razak, Z. Lockman, A. Abdul Aziz, PLoS ONE 7, e50405 (2012). https://doi.org/10.1371/journal.pone.0050405
24. F.G. Svensson, E. Djurberg, S. Kim, G. Westin, L. Österlund, Langmuir 41, 28399 (2025). https://doi.org/10.1021/acs.langmuir.5c03385
25. S. Kumar, J. Pandey, R. Tripathi, S.R. Chauhan, ACS Omega 8, 27732 (2023). https://doi.org/10.1021/acsomega.3c03860
26. L.E. Greene, M. Law, J. Goldberger, F. Kim, J.C. Johnson, Y. Zhang, R.J. Saykally, P. Yang, Angew. Chem. Int. Ed. 42, 3031 (2003). https://doi.org/10.1002/anie.200351461
27. S. Xu, Y. Wei, M. Kirkham, J. Liu, W. Mai, D. Davidovic, R.L. Snyder, Z.L. Wang, J. Am. Chem. Soc. 130, 14958 (2008). https://doi.org/10.1021/ja806952j
28. S.M. Sayem, R.K. Hariharalakshmanan, E. Badradeen, S.E. Bourdo, T. Karabacak, Materials 17, 3716 (2024). https://doi.org/10.3390/ma17153716
29. A.A.M. Raub, J. Yunas, M.M. Noor, Sh. Nadzirah, H.E.Z. Abidin, B.Y. Majlis, C.A.T. Tee, K. Hayashi, Y. Takabayashi, H. Miyazaki, M.Z.M. Yusop, R. Latif, Surf. Interfaces 78, 108185 (2025). https://doi.org/10.1016/j.surfin.2025.108185
30. L. Vayssieres, Adv. Mater. 15, 464 (2003). https://doi.org/10.1002/adma.200390108
31. C.-W. Lin, D.-J. Ke, Y.-C. Chao, L. Chang, M.-H. Liang, Y.-T. Ho, J. Cryst. Growth 298, 472 (2007). https://doi.org/10.1016/j.jcrysgro.2006.10.139
32. A.B. Djurišić, Y.H. Leung, Small 2, 944 (2006). https://doi.org/10.1002/smll.200600134
33. K. Vanheusden, W.L. Warren, C.H. Seager, D.R. Tallant, J.A. Voigt, B.E. Gnade, J. Appl. Phys. 79, 7983 (1996). https://doi.org/10.1063/1.362349
34. T.C. Damen, S.P.S. Porto, B. Tell, Phys. Rev. 142, 570 (1966). https://doi.org/10.1103/PhysRev.142.570
35. H. Harima, J. Phys.: Condens. Matter 14, R967 (2002). https://doi.org/10.1088/0953-8984/14/38/201
36. R. Cuscó, E. Alarcón-Lladó, J. Ibáñez, L. Artús, J. Jiménez, B. Wang, M.J. Callahan, Phys. Rev. B 75, 165202 (2007). https://doi.org/10.1103/PhysRevB.75.165202
37. C.A. Arguello, D.L. Rousseau, S.P.S. Porto, Phys. Rev. 181, 1351 (1969). https://doi.org/10.1103/PhysRev.181.1351
38. C.F. Bohren, D.R. Huffman, Absorption and Scattering of Light by Small Particles (Wiley-VCH, Weinheim, 1998). https://doi.org/10.1002/9783527618156

39. D.H. Raguin, G.M. Morris, Appl. Opt. 32, 1154 (1993). https://doi.org/10.1364/AO.32.001154
40. E.B. Grann, M.G. Moharam, D.A. Pommet, J. Opt. Soc. Am. A 11, 2695 (1994). https://doi.org/10.1364/JOSAA.11.002695
41. M.J. Bergmann, Ü. Özgür, H.C. Casey, H.O. Everitt, J.F. Muth, Appl. Phys. Lett. 75, 67 (1999). https://doi.org/10.1063/1.124278
42. W.L. Bond, J. Appl. Phys. 36, 1674 (1965). https://doi.org/10.1063/1.1703106
43. P. Lalanne, D. Lemercier-Lalanne, J. Mod. Opt. 43, 2063 (1996). https://doi.org/10.1080/09500349608232871

Figures

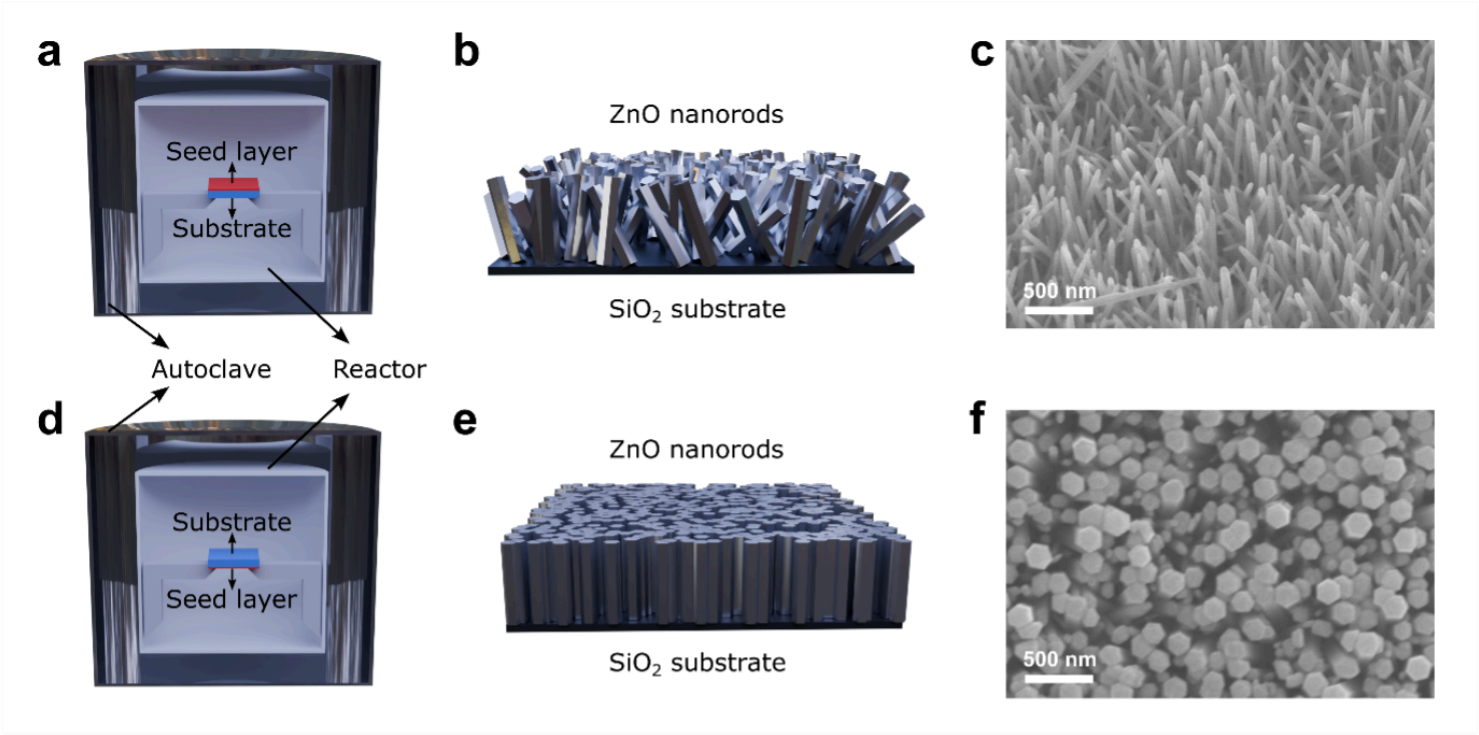


Figure 1

Synthesis and surface morphology of ZnO nanorods grown on SiO_2 substrates. (a) Schematic illustration of the hydrothermal synthesis with the seed layer facing upward inside the autoclave. (b) Schematic representation of randomly oriented ZnO nanorods on the SiO_2 substrate. (c) Perspective-view FE-SEM image of the ZnO nanorods synthesized with the seed layer facing upward. (d) Schematic illustration of the hydrothermal synthesis with the seed layer facing downward. (e) Schematic representation of vertically aligned ZnO nanorods on the SiO_2 substrate. (f) Top-view FE-SEM image of the ZnO nanorods synthesized with the seed layer facing downward. Scale bars, 500 nm

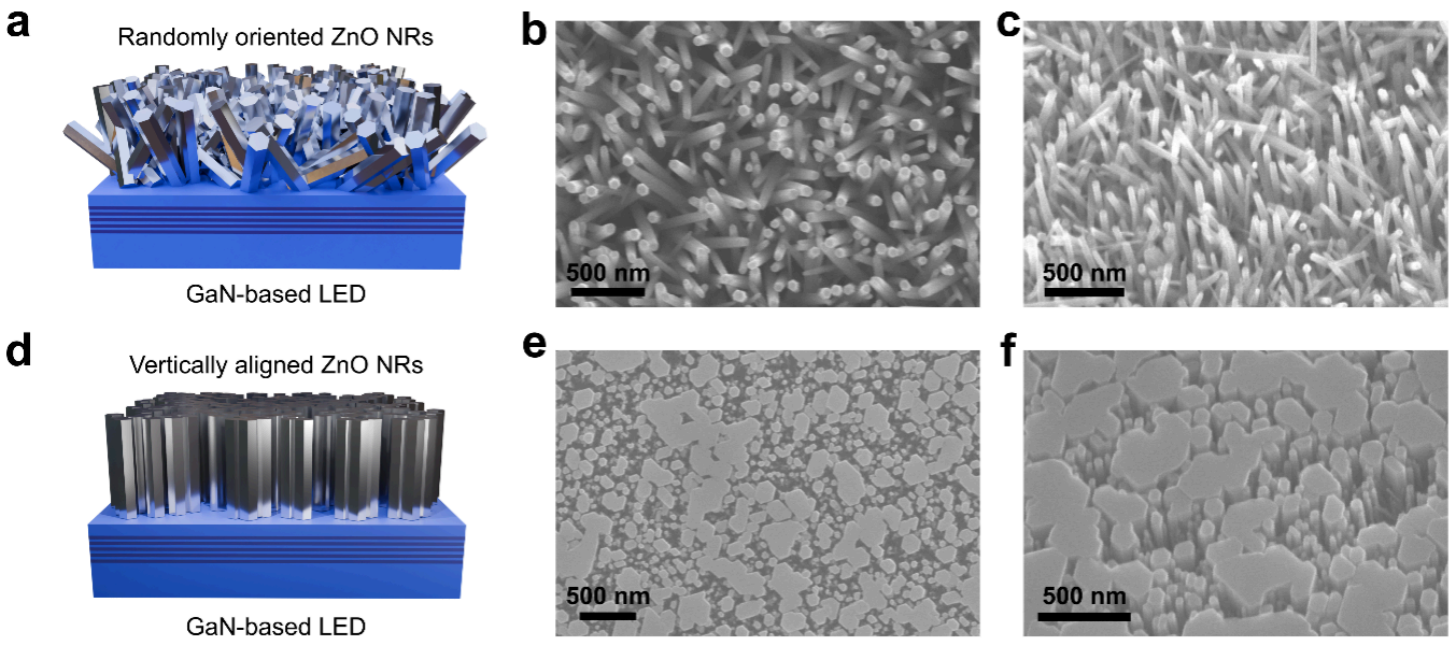


Figure 2

Growth and surface morphology of ZnO nanorods on a GaN-based LED substrate. (a) Schematic illustration of randomly oriented ZnO nanorods grown with the seed layer facing upward. (b) Top-view and (c) perspective-view FE-SEM images of the randomly oriented ZnO nanorods. (d) Schematic illustration of vertically aligned ZnO nanorods grown with the seed layer facing downward. (e) Top-view and (f) perspective-view FE-SEM images of the vertically aligned ZnO nanorods. Scale bars, 500 nm

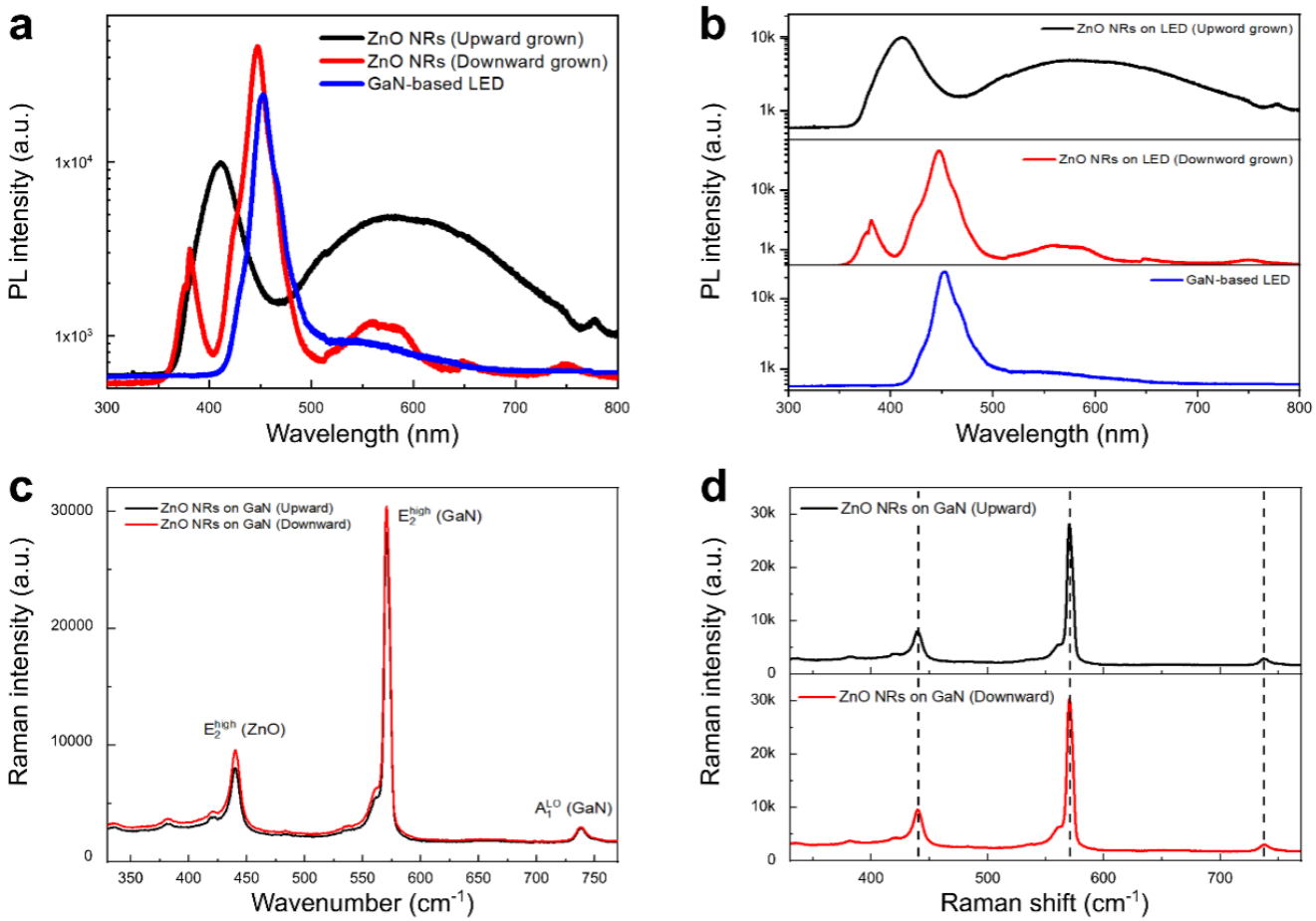


Figure 3

Optical and structural characterization of ZnO nanorods grown on a GaN-based LED substrate. (a) PL spectra of ZnO nanorods synthesized with different seed-layer loading directions, compared with the emission spectrum of the bare GaN-based LED. (b) Individual PL spectra of the upward-grown and downward-grown ZnO nanorods together with the GaN-based LED emission. (c) Raman spectra of the ZnO nanorods synthesized with different seed-layer loading directions. (d) Individual Raman spectra of the upward-grown and downward-grown ZnO nanorods

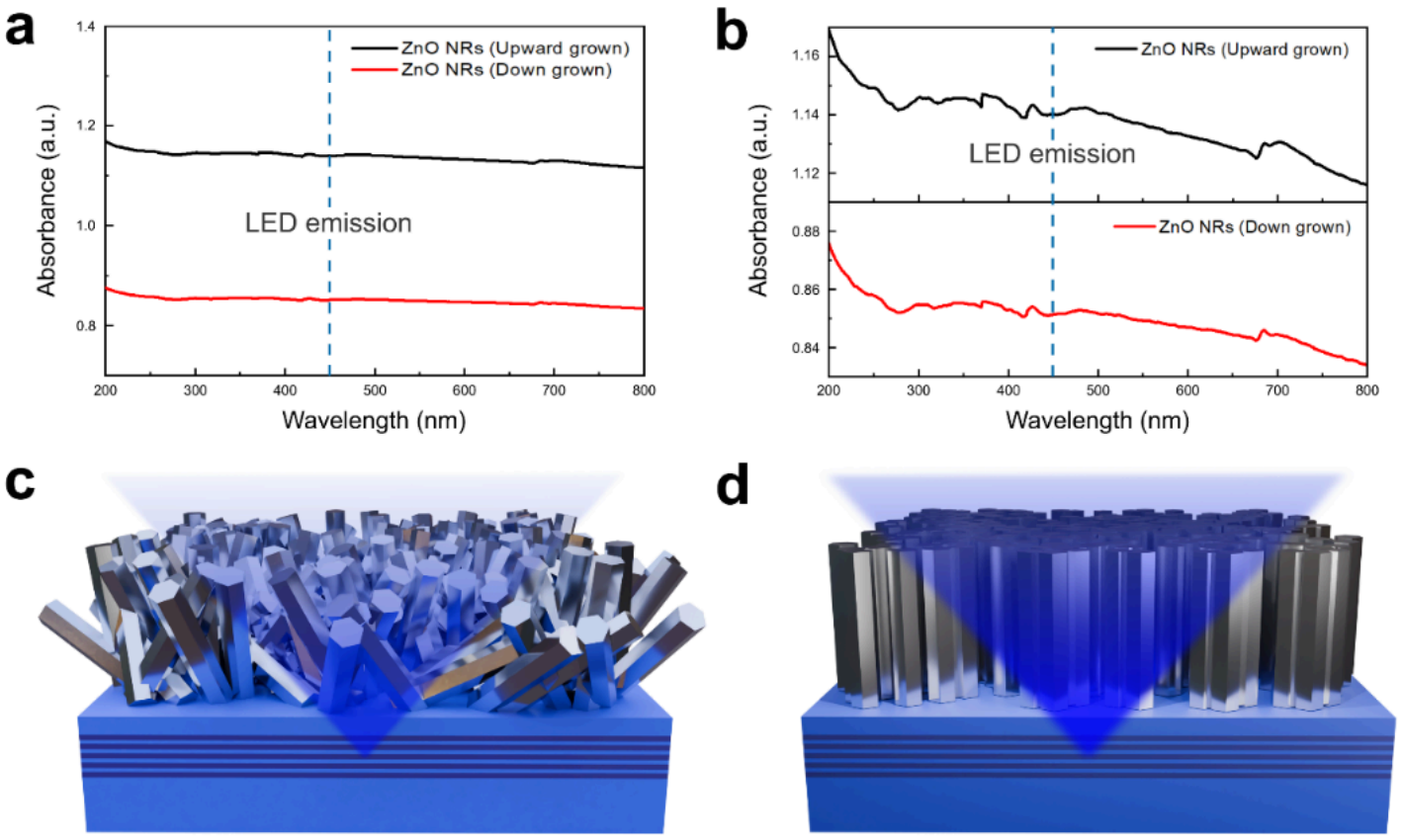


Figure 4

Optical absorption characteristics of ZnO nanorods synthesized with different seed-layer loading directions. (a) Absorbance spectra of the upward-grown and downward-grown ZnO nanorods over the 200–800 nm range. The dashed line indicates the emission wavelength of the GaN-based LED. (b) Magnified absorbance spectra around the LED emission wavelength. (c) Schematic illustration of light propagation through randomly oriented ZnO nanorods. (d) Schematic illustration of light propagation through vertically aligned ZnO nanorods

Supplementary Files

This is a list of supplementary files associated with this preprint. Click to download.

- SupplementaryMaterial.docx